Structure
Article

Structural and Theoretical Studies Indicate that the Cylindrical Protease ClpP Samples Extended and Compact Conformations

Matthew S. Kimber,[1,6] Angela Yeou Hsiung Yu,[2,6] Mikael Borg,[2,3,5,6] Elisa Leung,[2] Hue Sun Chan,[2,3,4] and Walid A. Houry[2,*]
[1]Department of Molecular and Cellular Biology, University of Guelph, Guelph, ON N1G 2W1, Canada
[2]Department of Biochemistry
[3]Department of Molecular Genetics
University of Toronto, Toronto, ON M5S 1A8, Canada
[4]Department of Physics, University of Toronto, Toronto, ON M5S 1A7, Canada
[5]Present address: Bioinformatics Centre, Department of Biology, University of Copenhagen, Ole Maaloes Vej 5, 2200 Copenhagen N, Denmark
[6]These authors contributed equally to this work
*Correspondence: walid.houry@utoronto.ca
DOI 10.1016/j.str.2010.04.008

SUMMARY

The highly conserved ClpP protease consists of two heptameric rings that interact by the interdigitation of an α-helix β strand handle domain motif to form a tetradecameric cylinder. We previously proposed that protease dynamics results in the temporary unstructuring of interacting pairs of handle domains, opening transient equatorial side pores that allow for peptide egress. Here, we report the structure of an *Escherichia coli* ClpP mutant in which each opposing pair of protomers is linked by a disulfide bond. This structure resembles the compact structures of *Streptococcus pneumoniae*, *Mycobacterium tuberculosis*, and *Plasmodium falciparum* ClpPs, rather than the active, extended structures that have previously been determined for *E. coli* ClpPs. The structural data, along with normal mode analysis, support a model whereby the ClpP cylinder switches dynamically between an active extended state required for substrate degradation and an inactive compact state allowing peptide product release.

INTRODUCTION

The ClpP protease is a highly conserved serine protease found in bacteria and most eukaryotes. The *E. coli clpP* gene codes for a 207 amino acid protein (Figure 1A) where the first 14 residues form a pro sequence that is rapidly cleaved off autocatalytically to form the mature, active protease (Maurizi et al., 1990a, 1990b). The mature ClpP protomer can be structurally divided into the axial loop (residues 15–31 in *E. coli*), a head domain composed of residues 32–138 and 172–207, and a handle region (β strand 6 and α-helix E, residues 139–171) (Wang et al., 1997) (Figures 1A and 1B). ClpP assembles into a tetradecamer, with the 14 subunits in the ClpP oligomer arranged into two heptameric rings, forming a D_7 symmetric cylinder approximately 100 Å in both height and diameter (Wang et al., 1997). A large interior chamber (approximately 50 Å in diameter) contains the 14 active sites, whose catalytic triad is composed of Ser111, His136, and Asp185 (*E. coli* ClpP SwissProt numbering). The intraring contacts are mediated by the head domain and are predominantly hydrophobic in nature, while the interaction between the two ClpP rings is mediated mainly by the handle region. Surprisingly, truncations in the handle region do not result in the dissociation of the two rings, implying a high degree of plasticity of this region (Gribun et al., 2005). It was proposed that the interaction between the two ClpP rings is stabilized by charge-charge interactions contributed by residues of the head domains (Maurizi et al., 1998; Gribun et al., 2005).

Entry of protein substrates into the ClpP lumen occurs through the two axial pores. These pores are lined by flexible axial loops, which in some conformations form β hairpins that start from inside the ClpP cylinder, extend above the cylinder, and then double back to pack between symmetry related copies of helix αA on the surface of the heptameric ring (Figure 1B; see Figure S1A available online). These loops are observed in human (Kang et al., 2004), *S. pneumoniae* (Gribun et al., 2005), and in later *E. coli* ClpP structures (Bewley et al., 2006; Szyk and Maurizi, 2006). These axial loops gate the entry of substrates into the ClpP proteolytic chamber (Gribun et al., 2005; Bewley et al., 2006; Jennings et al., 2008a). The axial loops mediate the interaction of ClpP with its cognate ATPases (Gribun et al., 2005; Martin et al., 2008) and, hence, are important for ClpP function.

The structures of ClpP from six organisms have been experimentally determined and were found to be composed of highly similar protomers (Yu and Houry, 2007). However, we noted that they exhibit differences in oligomeric organization and can be grouped into two distinct structural states. The first state, observed for ClpP from *E. coli* (Wang et al., 1997; Bewley et al., 2006; Szyk and Maurizi, 2006), *Homo sapiens* mitochondria (Kang et al., 2004), and *Helicobacter pylori* (Kim and Kim, 2008), we term the extended state. In this state, the distance from the apical surface of one subunit in one ring to the apical surface of the opposing subunit in the second ring (excluding the N-terminal loops) is approximately 100 Å (Figure S1A). In this state, residues 139–150 are ordered and form β6 and the

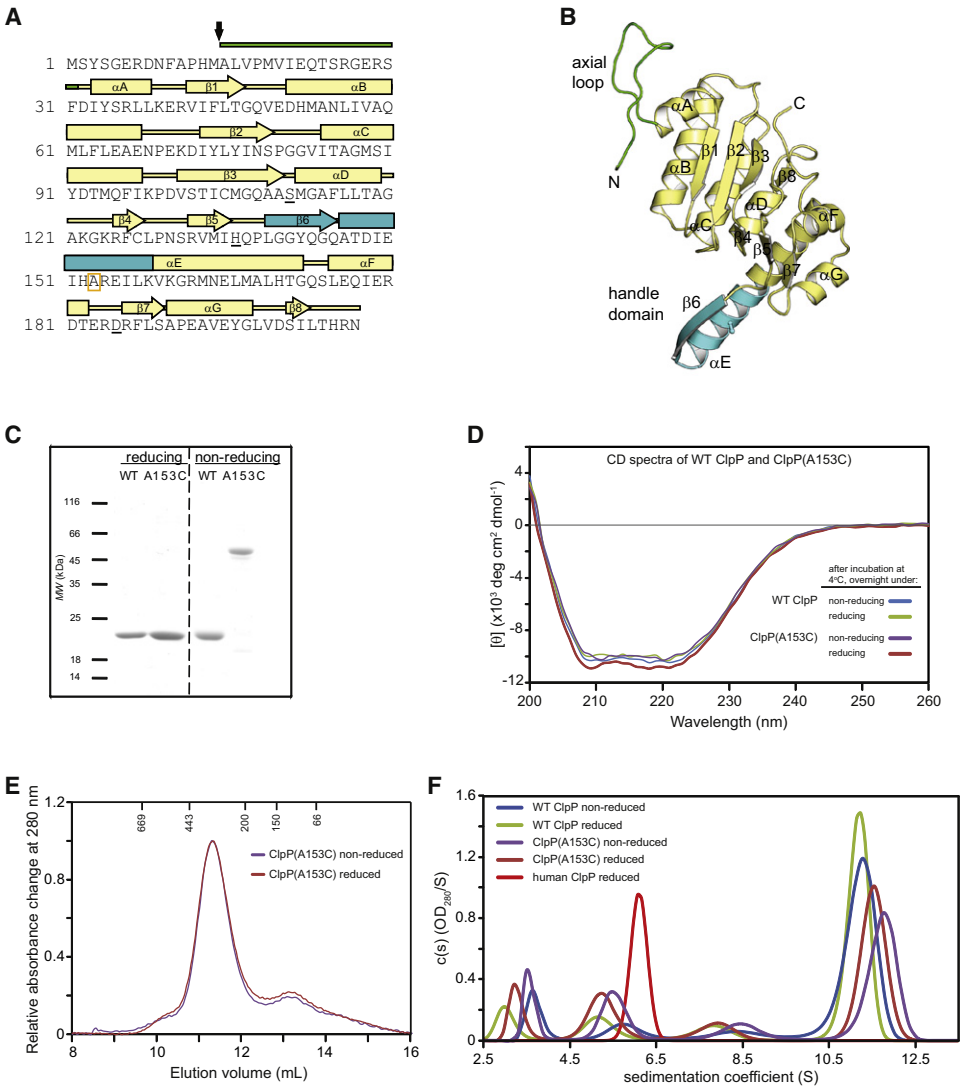

Figure 1. Biophysical Characterization of ClpP(A153C)

(A) The sequence and secondary structure of *E. coli* ClpP. The axial loop is colored green, the equatorial handle region cyan, and the head domain yellow. Ser111, His136, and Asp185 residues of the catalytic triad are underlined. Ala153 is boxed.

(B) Secondary structure elements of ClpP (1YG6), colored as described in (A). The side chain of Ala153 is shown in ball and stick representation.

(C) Mobility of WT ClpP and ClpP(A153C) in denaturing reducing and nonreducing gels.

(D) Far-UV CD spectra at 25°C of ClpP and ClpP(A153C) under reducing (+DTT) and nonreducing (no DTT) conditions.

(E) ClpP(A153C) under reducing and nonreducing conditions has similar elution profiles as observed by size exclusion chromatography using a calibrated Superdex 200 HR 10/30 column equilibrated ± DTT at 4°C.

(F) Profiles obtained from fitting the sedimentation velocity analytical ultracentrifugation data for WT and A153C *E. coli* ClpP and human mitochondrial ClpP to a continuous distribution model c(s) versus sedimentation coefficients in Svedberg units (S).

N-terminal end of αE of the handle domain; these residues from opposing rings interlock to form a continuous, unbroken surface at the ClpP equator. The catalytic triad in the extended state is generally organized in a catalytically competent, or near competent configuration. A second state, observed in the ClpP structures from *S. pneumoniae* (Gribun et al., 2005), *P. falciparum* (Vedadi et al., 2007), and *M. tuberculosis* (Ingvarsson et al., 2007), we term the compact state (Figure S1B). In this state, residues 139–150 are typically disordered, with residual electron density generally indicating that these residues occupy the lumen of the ClpP cylinder. The opposing rings are shifted closer together by a screw-like motion which slides the surfaces of opposing αE helices over one another, resulting in the opposing apical surfaces being approximately 10 Å closer. The component residues of the catalytic triad in these structures are disorganized, which, coupled with the disordered β6 guide strand, indicates that this structure likely corresponds to a catalytically inactive state of ClpP. It is worth noting that, to date, there is no firm experimental data showing that both states are accessible to a given ClpP from a specific species.

Table 1. Results of the Sedimentation Velocity Analytical Ultracentrifugation Experiments

		$s_{20,w}$ (S)	*MW* (kDa)	Percentage of Total for Major Species
WT ClpP	Reduced	11.6	287	71
	Nonreduced	11.7	288	74
ClpP(A153C)	Reduced	12.0	346	55
	Nonreduced	12.2	308	56
Human ClpP	Reduced	6.3	139	90

The table lists the solvent corrected sedimentation coefficients, $s_{20,w}$, at maximum c(s) as well as the corresponding apparent molecular weight of the major species observed obtained from fitting the sedimentation velocity analytical ultracentrifugation data (Figure 1F). The percentage of total for the major species observed is also given for each of the samples.

Table 2. Peptidase Activity of WT ClpP and ClpP(A153C)

		K_M (mM)	k_{cat} (min^{-1}) per Protomer
WT ClpP	Reducing	1.0 ± 0.1	15.8 ± 1.0
	Nonreducing	0.8 ± 0.1	9.6 ± 0.3
ClpP(A153C)	Reducing	1.1 ± 0.1	0.5 ± 0.1
	Nonreducing	Inactive	Inactive

K_M and k_{cat} for the cleavage of Suc-LY-AMC fluorogenic peptide were measured after incubation at 4°C overnight under reducing or nonreducing conditions.

ClpP on its own can efficiently degrade small peptides (Thompson and Maurizi, 1994; Thompson et al., 1994) as well as very slowly degrade poorly folded proteins (Jennings et al., 2008b; Bewley et al., 2009). The enzyme processively cleaves substrate proteins into peptides of seven to eight residues, which are then released from the chamber (Choi and Licht, 2005; Licht and Lee, 2008). The release mechanism is still under investigation. One model proposes that degraded products exit the ClpP proteolytic chamber by the same axial pores that allow polypeptide entry by passive diffusion (Thompson and Maurizi, 1994; Thompson et al., 1994). A second model, which we put forward, proposes that peptides are released through side pores that transiently form at the interface between the two heptameric ClpP rings by localized unfolding of pairs of interacting handle domains (Gribun et al., 2005; Sprangers et al., 2005).

In this study, we determined the structure of a crosslinked *E. coli* ClpP in which the two heptameric rings of ClpP are held together by disulfide bonds. Surprisingly, while all *E. coli* ClpP structures solved to date are in the extended state, the crosslinked ClpP structure was found to be in the compact state. Based on structural analysis and theoretical considerations, we propose that the ClpP compact state is naturally sampled by the protease in the course of its dynamics and that this state is functionally important, possibly for promoting degraded product exit from the protease catalytic chamber in the presence of the cognate chaperone.

RESULTS AND DISCUSSION

Biochemical Characterization of Disulfide Crosslinked ClpP

In a mutant variant of ClpP where A153 in helix αE of ClpP (Figure 1B) is mutated to cysteine, the introduced cysteines of two ClpP subunits from opposite rings readily oxidize, in the absence of reducing agent, to form a disulfide crosslinked ClpP(A153C) (Figure 1C). The overall secondary structure content of ClpP(A153C) is very similar to that of WT ClpP under reducing and nonreducing conditions as deduced from circular dichroism (CD) spectroscopy at 4°C (Figure 1D). Furthermore, reduced and nonreduced ClpP(A153C) migrate at around 300 kDa as observed by size exclusion chromatography at 4°C (Figure 1E), which is close to the expected size of the tetradecamer. A more careful analysis of the oligomerization of the protease at 20°C by sedimentation velocity analytical ultracentrifugation (AUC) indicates the presence of multiple oligomeric solution states for WT and mutant ClpP under reducing and nonreducing conditions (Figure 1F). However, the main species observed have a measured molecular weight of 287–346 kDa (Table 1), which is close to the theoretical molecular weight of ClpP tetradecamer of 302 kDa. The sedimentation coefficients obtained, $s_{20,w}$, for the main species are also consistent with a tetradecameric oligomer (Table 1). Hence, it can be concluded that the main oligomeric form of ClpP and ClpP(A153C) under reducing and nonreducing solution conditions is the tetradecamer. Human mitochondrial ClpP, which is known to form a single heptameric ring in solution (Kang et al., 2005), was used as a control in the AUC experiments (Figure 1F and Table 1).

Under reducing conditions, in which the disulfide bonds are not formed, ClpP(A153C) peptidase activity against the fluorogenic peptide *N*-succinyl-Leu-Tyr-7-amino-4-methyl-coumarin (Suc-LY-AMC) has a similar K_M but a 32-fold lower k_{cat} compared with that of WT ClpP (Table 2). This seems to indicate that the A153C mutation does not affect the substrate binding site but does affect the conformation of the active site of the protease. Alternatively, ClpP might be in equilibrium between an active and inactive conformation, and the mutation pushes the equilibrium toward the inactive state (see below). In the absence of DTT, the K_M for WT ClpP is unaffected, while the k_{cat} is reduced by about 1.6-fold compared with the values obtained in the presence of DTT (Table 2). The enhancement in WT ClpP activity by DTT seems to be caused by a nonthiol mediated side effect of DTT (Alliegro, 2000) (data not shown). The disulfide crosslinked ClpP(A153C) formed in the absence of DTT has no detectable peptidolytic activity (Table 2). This could be due either to a local rearrangement of the active site, which is located at the base of the handle region, or to a more global, although subtle, effect on ClpP structure. Consistent with the above observations, in the presence of the cognate chaperone ClpX, disulfide crosslinked ClpP(A153C) does not degrade GFP-SsrA model substrate (data not shown; see also Sprangers et al., 2005). Furthermore, in the presence of ClpA, the rate of degradation of the poorly structured model substrate casein by ClpP(A153C) is abolished under nonreducing conditions and is lower than that of WT ClpP under reducing conditions (Figures 2A and 2B). Note that, as observed for the peptidase activity (Table 2), the proteinase activity of WT ClpP is enhanced in the presence of DTT (Figures 2A and 2B).

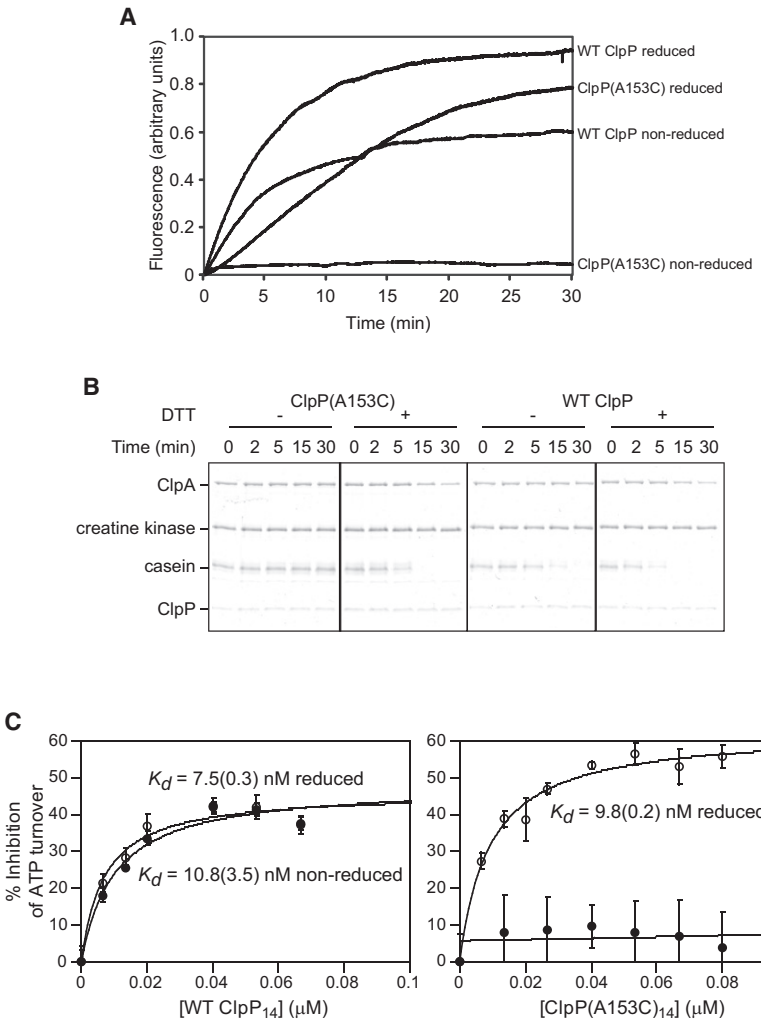

Figure 2. Binding of ClpP(A153C) to the AAA+ Chaperones

(A) The degradation of FITC-labeled casein by WT ClpP or ClpP(A153C) under reducing and nonreducing conditions in the presence of ClpA is shown as monitored by fluorescence.

(B) The degradation of α-casein by WT ClpP or ClpP(A153C) under reducing and nonreducing conditions in the presence of ClpA is shown on SDS-PAGE gels. The autodegradation of ClpA under reducing conditions can be observed at later time points.

(C) The inhibition of ClpX ATPase activity by WT ClpP or ClpP(A153C) under reducing (open circles) and nonreducing (closed circles) conditions is shown. Data points are averages of three repeats. The data were fit to a single-site Langmuir binding isotherm (solid lines) to obtain apparent binding constants. Numbers in parenthesis refer to standard deviations of at least three experiments. The measured ATPase activity of ClpX in the absence of the protease is 233 (±10) pmol min^{-1} μg^{-1} under reducing and nonreducing conditions.

The interaction of ClpP(A153C) with ClpX was assessed by measuring the ATPase activity of ClpX in the presence of increasing amounts of ClpP. It is known that ClpP inhibits ClpX ATPase activity (Wojtyra et al., 2003; Joshi et al., 2004). Fitting the data to a simple single-site Langmuir binding isotherm indicates that binding of ClpP(A153C) to ClpX under reducing conditions is similar to that of WT ClpP under reducing and nonreducing conditions (Figure 2C). However, ClpP(A153C) does not bind (or very weakly binds) ClpX under nonreducing conditions (Figure 2C).

The results shown in Figures 1 and 2 suggest that ClpP(A153C) under nonreducing conditions is an inactive protease that does not bind its cognate chaperone.

X-ray Structure of Disulfide Crosslinked ClpP

In order to gain further understanding of the conformational changes in ClpP, we determined the X-ray crystal structure of ClpP(A153C) under nonreducing conditions. We will refer to disulfide crosslinked *E. coli* ClpP(A153C) as ClpP^{SS}.

The structure of ClpP^{SS} was determined at 3.2 Å resolution. Table 3 lists the data collection statistics and the final refinement statistics. There are 28 chains, comprising two complete tetradecamers, in the asymmetric unit, along with fourteen well-ordered Ca^{2+} ions that predominantly mediate crystal contacts. At 3.2 Å resolution, some details are difficult to discern; nevertheless, the broad features of the structure are readily apparent. The structure interpretation is helped by the availability of high-resolution model structures to guide the correct placement of the side chains even where the electron density is ambiguous. Furthermore, given the high solvent content of this crystal form (72%), there are four reflections per atom, a ratio more typical of a 2.7 Å structure. Finally, having 28 independent copies in two tetradecamers allows multiple independent views of each detail, greatly improving the reliability of the interpretation. At minimum, residues 32–137 and 153–207 are built for all monomers, though details vary by chain (Table S1).

Disulfide crosslinking appears to minimally perturb the protomer structure, and individual monomers of ClpP^{SS} superpose well with the protomer structures previously determined for WT *E. coli* ClpP (~0.4 Å rmsd) (Figure 3A, protomers on left), although there is some structural heterogeneity among different ClpP^{SS} protomers (Figure S2A). Among the more notable local changes is a significant bending of αE, as well as the disorder of residues Pro138 to Cys153, though some protomers have a few more residues ordered. The electron density map clearly shows that Cys153 in each monomer forms a disulfide bridge with the corresponding residue in the opposite ring (Figure 3B). Crosslinking appears to predominantly induce significant changes within the oligomeric structure at two levels. First, packing within the ring is subtly changed, with each protomer translated inward toward the sevenfold axis by as much as 1 Å (Figure 3A, protomers on right). Note that comparisons of all *E. coli* ClpP ring structures shows that some variations occur between the structures, but ClpP^{SS} represents an extreme

Table 3. Data Collection and Structure Refinement Statistics

Data Collection Statistics	
Temperature	100 K
Space group	$P3_221$
Cell dimensions	a = b = 182.30 Å c = 476.86 Å
Wavelength (Å)	1.0000
Resolution (Å)	40.0–3.2
Total observations	437604
Unique observations	148306
Completeness (last shell)[a]	0.975 (0.917)
$<I/\sigma(I)>$ (last shell)[a]	14.2 (2.1)
R_{sym} (last shell)[a]	0.045 (0.394)
Refinement statistics	
Resolution range (Å)	40–3.2
Asymmetric unit contents	
Chains	28
Ca^{2+}	14
R_{cryst}	0.213
R_{free}[b]	0.253
rmsd bond lengths (Å)	0.007
rmsd bond angles (°)	0.99
Ramachandran plot	
Most favorable (%)	94.6
Additionally allowed (%)	4.9

[a] The last shell includes all reflections between 3.31 and 3.20 Å.
[b] R_{free} calculated using 5% of the data which were chosen randomly.

case (Figure S2B). Second, all *E. coli* ClpP structures solved to date exhibit the extended form; the compact conformation has never before been observed for the *E. coli* protease. Here, the structure of $ClpP^{SS}$ is clearly in the compact form, adopting a conformation closely resembling the previously determined structures of *S. pneumoniae* and *P. falciparum* ClpP (Figure 3C). (The *M. tuberculosis* ClpP is also in a compact conformation, but the protomers within a ring are rotated outward, making detailed comparisons difficult.) The similarity of these three compact structures is interesting as they involve three different sequences with different modifications: A153C oxidized, A153P (using *E. coli* SwissProt sequence numbering), and WT for *E. coli*, *S. pneumoniae*, and *P. falciparum*, respectively. The structural similarities suggest that this is a naturally occurring, low energy structural state for ClpP. For $ClpP^{SS}$ in particular, the concerted structural and functional changes observed as the protein is switched from reducing to oxidizing conditions argue that the *E. coli* ClpP protein must have an innate ability to switch between these states.

The structure of $ClpP^{SS}$ contrasts markedly with the extended tetradecameric structure seen in all previous *E. coli* ClpP structures (Figure S1A), as well as the similarly extended *H. pylori* and human mitochondrial ClpP structures. In the $ClpP^{SS}$ tetradecamer structure, the two opposite rings are shifted approximately 4 Å closer relative to WT *E. coli* ClpP, and one ring is rotated approximately 5° around the 7-fold NCS axis. Collectively, this motion can be visualized as a screw-like motion generated by the sliding of the equatorial helices αE approximately one full turn along their length toward the opposite subunit (Figure 3B). These rearrangements also result in the catalytic site being disorganized similar to what is also observed for *S. pneumoniae* ClpP(A153P), *M. tuberculosis* ClpP, and *P. falciparum* ClpP, while WT *E. coli* ClpP structures show that the active site is well organized (Figure S3). This reinforces the idea that the compact conformation is accompanied by the formation of an inactive arrangement in the catalytic site. This is the first instance in which the extended and compact forms are observed for ClpP from the same organism.

As mentioned earlier, the N-terminal axial loop is composed of residues 15–31 (Figures 1A and 1B). Residues 22–31 are hydrophilic and form a loop that extends out from the pore above the heptameric ring surface; these extended hydrophilic loops appear to be only weakly structured, being either too disordered to trace in electron density maps, or stabilized in a variety of conformations by crystal packing and other interactions (Gribun et al., 2005; Bewley et al., 2006; Szyk and Maurizi, 2006). Residues 15–21 are hydrophobic and anchor the N terminus of the axial loop to the head domain mainly by the placement of the side chains of Pro18 and Val20 in a shallow hydrophobic groove formed predominantly by the residues at the N terminus of αA from two adjacent protomers (Figure 3D). Examination of the electron density map clearly indicates that all axial loops are wholly disordered in $ClpP^{SS}$, with the last ordered residue being Asp32. The absence of clear electron density in this region could, in principle, be due to the 3.2 Å resolution of the electron density maps combined with the intrinsically high temperature factors for these residues as observed in other ClpP structures. However, difference maps contoured at 0.5 σ show no plausible density in the appropriate region for residues N-terminal to Phe31 in any subunit, and no peptide-like density was found in the grooves between the αA helices of adjacent monomers (Figure S4).

While the axial loops have some plasticity in all ClpP structures solved to date, adopting different conformations in different protomers even when ordered, this plasticity is found N-terminal to Phe31. Phe31 itself in WT ClpP structures is typically held in place by packing the phenyl ring against the side chains of Tyr34 and Ser35 of helix αA of the same subunit, as well as Met19 and Ile21 of the neighboring subunit (Figure 3D). *B*-factors for Phe31 in published *E. coli* WT ClpP structures are similar to the overall chain average. Inspection of all 28 copies of $ClpP^{SS}$ subunits in the asymmetric unit revealed no electron density consistent with Phe31 packing in this fashion (Figure 3D). Density for this residue in $ClpP^{SS}$ is very weak, with strong indications of disorder, but some monomers show hints that this residue may form a continuation of helix αA, in a manner analogous to the *M. tuberculosis* (2CE3) (Ingvarsson et al., 2007) and *P. falciparum* ClpP (2F6I) (Vedadi et al., 2007) structures. Since both of these structures are in the compact state, this suggests that the heptameric ring in the compact conformation may be at least partially coupled to structural changes in the axial loops. In $ClpP^{SS}$, the disorder in the N-terminal loops appears to correlate with shifts of the protomers within each heptameric ring, one effect of which is to bring the adjacent αA helices slightly closer together. This pinches closed the hydrophobic grooves in which the very N-terminal residues (typically Pro18 and Val20) of the axial loops bind, leading to the disordering of these residues (Figure 3D).

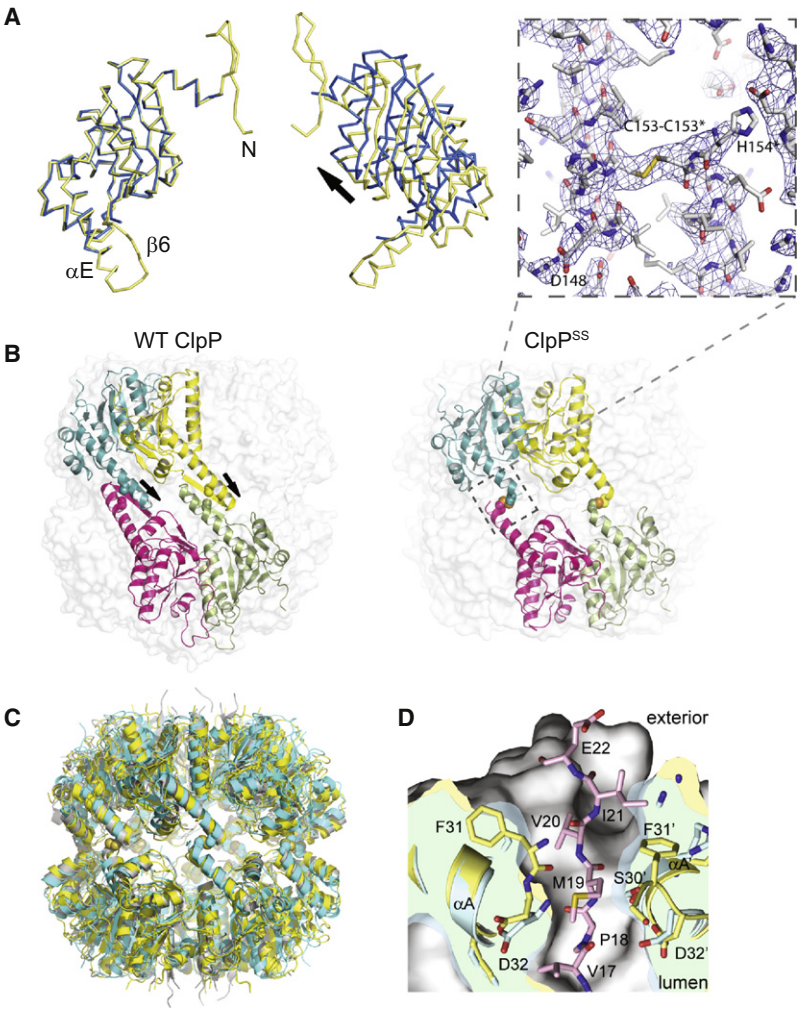

Figure 3. The Overall Structure of ClpP^{SS} and Comparison with WT ClpP

(A) The protomers on the left show the superposition of a single subunit of ClpP^{SS} (blue) on WT ClpP (yellow, 1YG6). On the right are protomers from the opposite side of the heptameric ring. Arrow here and arrows in (B) show the direction of protomer motion from the extended to the compact conformations.

(B) Structure of *E. coli* ClpP^{SS} showing four monomers as cartoon traces with Cys153 represented as spheres. A surface trace for the entire tetradecamer is also shown. In ClpP^{SS}, β6 and two turns of the αE helix are completely disordered. For comparison, WT *E. coli* ClpP (1YG6) is also shown with Ala153 drawn as spheres. The magnified area depicts the $2mF_o$-DF_c electron density map, contoured at 1.0 σ, showing the handle region viewed from inside the ring. Electron density corresponding to the disulfide bond is clear in all 14 interring disulfide bonds (not shown).

(C) Superposition of the *E. coli* ClpP^{SS} tetradecamer (cyan cartoon with residue 153 in sphere representation) on the ClpP structures from *S. pneumoniae* (gray, 1Y7O) and *P. falciparum* (yellow, 2F6I). Only the lower ring was used for superposition. In general, single rings in all three structures superpose well, but there are minor differences in the degree to which the rings approach one another, with ClpP^{SS} being the least compact.

(D) WT *E. coli* ClpP is shown (2FZS) as a gray surface, showing yellow where it is sliced through in the plane of the page at the level of the Val20 side chain. The corresponding footprint of the ClpP^{SS} surface in the same plane is overlain as a semitransparent pale blue surface. Cartoon and stick representations for selected residues that protrude above this surface are in yellow (WT) and pale blue (ClpP^{SS}). Residues 17–22 of WT ClpP, in pink, bind in the groove between adjacent copies of the helix αA. The domain shifts in ClpP^{SS} pinch closed this groove, disrupting the binding surface of the axial loop that anchors the loop to the protease apical surface resulting in a disordered loop. See also Figure S1 to S4 and Table S1.

Protomer rotations within the ring provide a mechanism to couple the disulfide crosslinking of axial helices to disorder of the axial loops, and this would result in the loss or reduction of the interaction between ClpP and its cognate ATPase chaperones, which is consistent with the binding data of Figure 2C. This suggests a possible general mechanism by which ClpP coordinates events at the axial pores and the equatorial helices.

Normal Mode Analysis Suggests that the Structure of ClpP^{SS} Corresponds to a Naturally Sampled Conformation of WT ClpP

In order to further analyze the compact ClpP^{SS} structure and its relation to the extended ClpP structures, we performed normal mode analysis (NMA) using the elastic network model (ENM) (Tirion, 1996; Bahar et al., 1997; Hinsen, 1998). In brief, ENM is a framework for calculating collective motions in biomolecules by assuming a simple network of springs between atoms closer than a specified cutoff distance. The normal modes are then calculated as the eigenvectors of the Hessian matrix that corresponds to perturbations of the input structure. This methodology is widely used for analyzing collective motions, residue fluctuations, and conformational changes of proteins (Case, 1994; Ma, 2005; Yang et al., 2008). The structures that we used for this analysis are as follows: PDB codes 1TYF (Wang et al., 1997), 1YG6 (Bewley et al., 2006), 1YG8 (V20A mutant) (Bewley et al., 2006), and 2FZS (ClpP containing a covalently bound inhibitor) (Szyk and Maurizi, 2006). Multiple structures were selected to ensure that the results obtained are not specific to one ClpP structure in the PDB but are rather generally applicable. We will collectively refer to these previously solved *E. coli* ClpP structures as the extended ClpP structures, ClpP^{ex}. Normal mode analysis was not carried out on the ClpP^{SS} structure since missing residues in the unstructured equatorial region resulted in unrealistic normal modes.

We calculated the 100 lowest frequency eigenmodes of ClpP^{ex} (1TYF, 1YG6, 1YG8, and 2FZS with inhibitor excluded) using the NOMAD web server (Lindahl et al., 2006), with the default settings of a distance weight parameter (Hinsen, 1998) of 5 Å and a cutoff of 10 Å, and including all atoms in the structures. The six slowest eigenmodes correspond to rigid translations and rotations and were discarded. In order to compare the solved structures of ClpP^{ex} to the current ClpP^{SS} structure, we calculated the overlap between each eigenmode of ClpP^{ex} and the difference vectors, Δq, between the atoms in the

experimental structures of ClpP^{SS} (using the tetradecamer with chains O–Z and 1–2; similar results were obtained when using the other tetradecamer in the unit cell, chains A-N) and ClpP^{ex}. The overlap, I_j, was calculated as in (Marques and Sanejouand, 1995):

$$I_j = \frac{\sum_i |u_{i,j}\Delta q_i|}{\sqrt{\sum_i u_{i,j}^2 \sum_i \Delta q_i^2}} \quad (1)$$

where $u_{i,j}$ is the displacement vector of atom i for eigenmode j. The overlap is a measure of whether a given eigenmode can drive the two structures to a lower rmsd distance. The result from this calculation, shown in Figure 4A, shows that, in all cases, the highest overlap has an I_j of about 40%. The highest overlap mode is the fifth slowest mode, mode 11, which, for the different structures considered, corresponds to very similar but not identical motions. For all four structures, mode 11 is a breathing motion accompanied with a twisting motion. The twisting motion is more accentuated for 1YG8 and 2FZS (Movies S1–S4). The ClpP dynamics based on mode 11 for 1YG6, shown in Movie S1A (side view), is predominantly a breathing motion of the two heptameric rings along the longitudinal axis of the full structure in conjunction with a slight twist. The motion perturbs the equatorial region and suggests the possibility of pores forming. This is more evident in Movie S1B, where we show a cross section of the same motion. The size of the axial pores also changes considerably in this eigenmode, as shown in the top view (Movie S1C). In Movie S1D, the eigenmode 11 motion is shown for one heptameric unit, viewed from the inside of the catalytic chamber toward the axial pore. Most of the displacements in the structure appear to result from the subunits moving relative to one another.

We also compared the eigenmodes from the different ClpP^{ex} structures by calculating the overlaps between the eigenmode vectors, $|u_k v_l|/(|u_k||v_l|)$ where u_k (v_l) is the k^{th} (l^{th}) eigenvector of structure u (v). For these calculations, we used the Cα displacement vectors. In Figure 4B, the eigenvector overlaps are shown in the form of matrix scatter plots, where the color of each pixel with matrix index (k, l) represents the overlap between modes k and l. The results show a very high degree of similarity between the eigenmodes of the different structures, which is to be expected, as the structures are very similar. In particular, the eigenvectors of mode 11 from 1TYF and 1YG6 are virtually identical (overlaps ~0.99). Furthermore, mode 11 of 1TYF and 1YG6 is very similar to mode 12 of 1YG8 and 2FZS (overlaps ~0.8), but there is also appreciable overlap with mode 11 (~0.5–0.6) of 1YG8 and 2FZS.

Even though the elastic network model has been shown to be surprisingly accurate despite its simplicity (Bahar et al., 1997; Atilgan et al., 2001; Bahar and Rader, 2005), it is important to note that the collective motions and frequencies rely on a harmonic approximation of the forces. The amplitudes of the motions depend not only on the eigenfrequencies, but also on temperature, initial conditions, and on the effects of crystal structure and solvent (Hinsen, 2008). In our case, the normal mode analysis is further complicated by the fact that some amino acids are missing in the experimental structures, which can result in wrong eigenfrequencies and spurious eigenmodes. Some of the motions found by the analysis may be unrealistic due to steric hindrance, which is not taken into account in the NMA calculations. In order to get an indication of the importance of the individual modes, we used the information contained in the B-factors of the experimental crystal structures. We fit the amplitudes of the displacements individually in the form of a weight, w_j, attributed to each mode, to the experimental temperature factors. The temperature factors, B_i, are given as:

$$B_i = 8\pi^2 \langle \Delta r_i^2 \rangle \quad (2)$$

where $\langle \Delta r_i^2 \rangle$ is the mean square displacement of atom i, which is related to the eigenmode displacements through (Brooks et al., 1995):

$$\langle \Delta r_i^2 \rangle = \sum_j w_j |u_{i,j}|^2 \quad (3)$$

where $u_{i,j}$ is the eigenvector of mode j. In this formulation, the set of eigenmodes is viewed as a basis set, and the weights w_j are then fit to achieve the best agreement with the experimental temperature factors using nonnegative least square minimization (Lawson, 1974) of $\left\{ |B_{exp} - B_{calc}|^2 \right\}$. The result of this calculation shows that most of the thermal motions can be attributed to the slowest 16 eigenmodes (modes 7– 22), with the fifth slowest mode, mode 11, making the highest contribution (Figure 4A), except for 2FZS where it is second highest. The Pearson's correlation coefficients between the experimental and fitted B-factors were 0.69, 0.66, 0.78, and 0.69 for 1TYF, 1YG6, 1YG8, and 2FZS, respectively. Our results can be compared to the average correlation of ~0.6 obtained using the Gaussian Network Model in a comparison between B_{exp} and B_{calc} for 113 protein structures (Kundu et al., 2002), where the authors scaled the amplitudes with the inverse of the eigenvalues (reciprocal of frequency squared) and fit the global amplitude scale to the experimental data (also see below).

The result of these calculations shows that in all cases except for 2FZS, the mode with the highest overlap is also the mode with the highest contribution to the temperature factors, providing key support to our hypothesis that the ClpP^{SS} structure can be viewed as a not-so-infrequent snapshot of the ClpP^{ex} structure undergoing thermal motions. The 2FZS structure has a covalently bound inhibitor at the active sites, which may influence the dynamics. The inhibitor was not included in the NMA calculation.

In order to further investigate the relationship between the WT and mutant ClpP structures, we calculated the all-atom rmsd distance between ClpP^{SS} and the normal-mode-perturbed conformations of ClpP^{ex}, for the different modes. The atomic positions, r_i, of the perturbed conformations were calculated as described previously (Marques and Sanejouand, 1995):

$$r_i = r_{0,i} + a_j u_{i,j} \sin\theta \quad (4)$$

where $r_{0,i}$ is the experimental position of the atom, a_j and $u_{i,j}$ are the amplitude and eigenmode vector of mode j, respectively, and θ is the phase factor, which describes the oscillations around the unperturbed structure. We then calculated the perturbed structures for each mode for different amplitudes and compared each of these structures with ClpP^{SS} structure using rmsd as a measure of similarity. The result of this calculation confirmed the result from the overlaps (Figure 4A): the motions of the modes

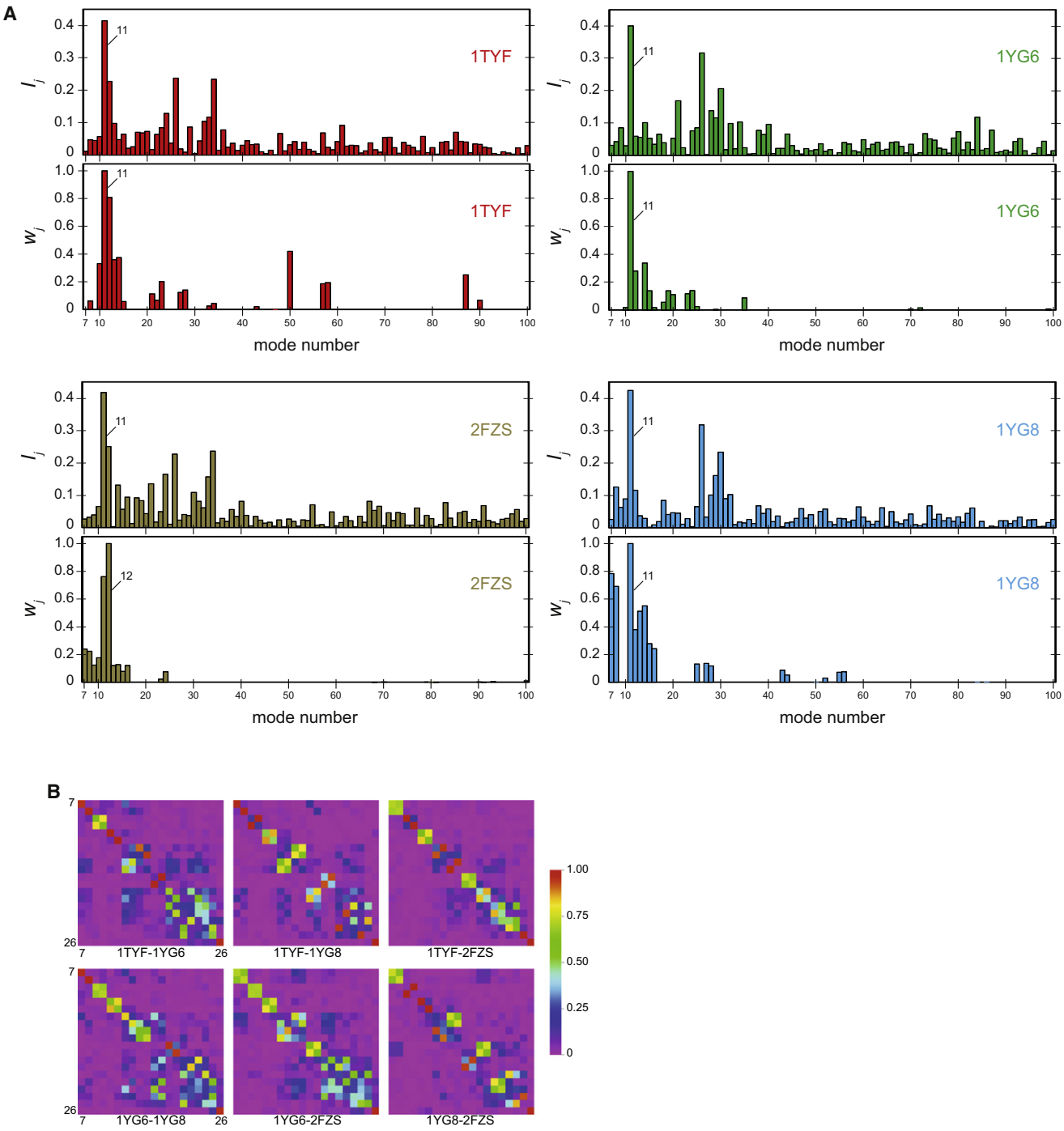

Figure 4. ENM Normal Mode Analysis of ClpP

(A) Shown are the overlaps I_j (top panels) and the eigenmode weights w_j (bottom panels) for each eigenmode of the extended ClpP structures 1TYF, 1YG6, 1YG8, and 2FZS.

(B) Scatter plots of the overlap of the eigenvectors between the extended ClpP structures. Each scatter plot shows the overlaps of the 20 slowest eigenvectors (modes 7–26) between the two structures indicated below the plot. The first six eigenvectors that correspond to rigid translations and rotations are excluded. The definition of overlap is given in the text. The color of a pixel in row k and column l represents the overlap between eigenvector k of the first structure and eigenvector l of the second structure. The row and column numbering is in matrix format, so that the top left corner corresponds to the slowest mode under consideration. The top row of the first scatter plot thus contains the overlap of mode 7 of 1TYF with modes 7, 8, … 26 of 1YG6. An overlap of 1 corresponds to identical eigenvectors. In some cases, similar eigenvectors have different eigenvalue ranks, which results in high intensity off-diagonal elements. For example, the fourth slowest mode of 1TYF is similar to the third slowest mode of 1YG8 which is visible as a bright pixel at row 4 column 3 in the second scatter plot (1TYF-1YG8). See also Movies S1 to S4.

with the highest overlap cause the structures of $ClpP^{ex}$ to become more similar to that of $ClpP^{SS}$. The experimental $ClpP^{SS}$ and the $ClpP^{ex}$ structures of 1TYF, 1YG6, 1YG8, and 2FZS differ by rmsd values of 3.61, 3.48, 3.06, and 3.35 Å, respectively. The optimal single normal mode perturbation decreased this value to a minimum of 3.00, 2.70, 2.09, and 2.18 Å, respectively.

As the amplitudes required for these motions were found numerically, we also checked whether the amplitudes are realistic. This was carried out by fitting the overall scale, *W*, of the motions to the experimental *B*-factors using the expression (Brooks et al., 1995):

$$B_i = W \sum_j u_{i,j}^2 / \rho_j^2 \quad (5)$$

where ρ_j is the frequency of eigenmode *j*. The relative contributions from the different modes to the *B*-factors are inversely proportional to the square of the eigenfrequencies. This would be the appropriate formulation consistent with equipartition of kinetic energy among eigenmodes if we could compute the physical eigenmodes of the structures. The value of *W* depends to some extent on the number of modes included in the fit. Here, we included all 94 nontrivial eigenmodes in order to get a rough estimate of *W*, even though the high frequency modes actually worsened the correlation between the calculated and the experimental *B*-factors. The result from this fit showed that the amplitudes of mode 11 were a factor of about 20 to 40 smaller than the optimal amplitudes. Using only the 16 slowest eigenmodes, they were a factor of 10 smaller. It should be noted that amplitudes fit to experimental *B*-factors were obtained from crystallized samples at ~100 K; thus, the corresponding amplitudes describing ClpP dynamics at ~300 K should be larger. Some of the eigenmodes may also be artifacts due to missing residues in the structures. Nonetheless, even taking these considerations into account, the amplitudes required for fitting the conformational difference between $ClpP^{ex}$ and $ClpP^{SS}$ are significantly larger than the amplitudes obtained from fitting the *B*-factors (Figure 4A). This implies that, if thermal vibrational motions embodied by mode 11 do bridge $ClpP^{ex}$ and $ClpP^{SS}$ as we propose here, the vibrational motion cannot be purely harmonic because the energy cost involved would be too high. Most likely the motion should pass over a barrier separating the $ClpP^{ex}$ and $ClpP^{SS}$ conformations which are situated at two different free energy minima.

This physical picture of ClpP dynamics is reminiscent of that provided by a straightforward anharmonic interpolation approach to model the "switching" barrier of an allosteric process (Miyashita et al., 2003b). In fact, intuitively, the average absolute values of atomic displacement corresponding to the optimal amplitudes are not large. For 1TYF, 1YG6, 1YG8, and 2FZS, the average of $a_j|u_{i,j}|$ over *i* for mode $j = 11$ (see Equation 4) for the optimal a_j are 1.77, 1.76, 1.90, and 2.15 Å, respectively. In light of the insights gained here, it will be extremely interesting for future investigations to study possible conformational and energetic pathways (Kim et al., 2002; Miyashita et al., 2003a) between the extended and compact states of ClpP.

Thus, in summary, the normal mode analysis of four extended ClpP structures shows that a few normal modes have appreciable overlap with the difference vectors to the compact $ClpP^{SS}$ structure. These high overlap modes coincide with the modes that best describe the experimental temperature factors of the extended structures, suggesting that the high overlap modes are likely the dominating large-scale motions. In this view, the $ClpP^{SS}$ structure is stipulated as a probable snapshot of $ClpP^{ex}$ undergoing thermal motion.

Conclusion

In conclusion, our current analysis of the $ClpP^{SS}$ structure provides new insights into the dynamics of this system. Our data support the view that ClpP undergoes several dynamic conformational changes that we propose are part of its functional cycle. Recently published biochemical data also support the presence of such conformational changes in ClpP (Maglica et al., 2009). Our X-ray structure of $ClpP^{SS}$ and normal mode analysis suggest that one dominant motion that ClpP might undergo is a compression motion that is accompanied with a slight rotation in which the two ClpP rings of the tetradecamer are brought closer together (Movies S1–S4). This should result in the reduction of the size of the catalytic chamber of ClpP. Since we had earlier proposed that degraded products are released from ClpP through the formation of transient equatorial side pores (Gribun et al., 2005; Sprangers et al., 2005), it might be reasonable to speculate that the compression motions depicted by mode 11 (Movies S1–S4) might actually allow the exit of the peptides generated after substrate degradation from the ClpP catalytic chamber. Importantly, if the $ClpP^{SS}$ structure represents a conformational state sampled not infrequently by the WT ClpP, then ClpP might undergo switching between an active extended state required for substrate degradation and an inactive compact state supporting product release. A bound ClpX or ClpA chaperone might modulate this conformational switching of ClpP using energy derived from ATP hydrolysis. It is interesting to note that the breathing motion accompanied by slight twisting observed for ClpP is similar to the motions of the slowest normal modes found for the GroEL-GroES complex (Ma et al., 2000; Keskin et al., 2002).

Other conformational states that, for example, allow substrate translocation into the ClpP chamber, and probably involve motions of the axial loops, must also be sampled by ClpP dynamics. Understanding the dynamics of this system is an important undertaking for gaining insights into its mechanism of function. Future studies will have to combine novel biophysical techniques including NMR spectroscopy and single molecule studies with theoretical considerations in order to properly describe the motions of the ClpP tetradecameric cylinder at the molecular level.

EXPERIMENTAL PROCEDURES

Protein purification and biophysical characterization were done following standard protocols. Details are provided in Supplemental Experimental Procedures. $ClpP^{SS}$ was crystallized by the sitting drop method with vapor diffusion using 1 μl of 23 mg/ml protein solution mixed with 1 μl of buffer (1 M 1,6-hexanediol, 0.1 M sodium acetate [pH 4.6], 10 mM $CoCl_2$, and 100 mM $CaCl_2$). The protein was equilibrated against the same buffer. Crystals grew as hexagonal bipyramids up to 1.2 mm in length. Crystals were gradually dehydrated by exposure to air prior to freezing in a 100 K nitrogen stream. X-ray diffraction data were collected at Advanced Photon Source (APS), Argonne National Laboratory (ANL) (Chicago, IL) on beamline 19ID and processed in HKL3000 (Minor et al., 2006). Diffraction data conformed to the trigonal space group

$P3_221$ with cell dimensions a = b = 182.30 Å and c = 476.86 Å. Despite the long c-axis, low mosaicity (0.47°) resulted in individual reflections being sharp and well resolved. Crystals diffracted X-rays to a maximal resolution of 3.2 Å. Data collection and model refinement statistics are reported in Table 3.

The structure was solved using Molrep in CCP4 (Collaborative Computational Project, 1994), searching with one heptameric ring from 2FZS (Szyk and Maurizi, 2006). Four such heptameric rings were found arranged as two tetradecamers, and individual domains were subjected to rigid body refinement. Despite the high solvent content (72%), no further heptameric rings could be found. Given the contiguous crystal lattice contacts in all directions and good refinement statistics for the final model, the structure is deemed to be complete. Refinement was performed using Refmac in CCP4 with each monomer refined as a single TLS (translation/libration/screw) group. Structure rebuilding was done in XtalView (McRee, 1999) and Coot (Emsley and Cowtan, 2004). NCS restraints were found to degrade the R_{free} and were not used in the refinement. Axial loop residues 15–31 were disordered in all structures. Most residues in the handle domain were disordered, typically residues 138–151, though the first disordered residue ranged from 137 to 141, and the last disordered residue between 147 and 152 (Table S1).

ACCESSION NUMBERS

The coordinates and structure factors for $ClpP^{SS}$ were deposited in the Protein Data Bank (PDB) with accession number 3HLN.

SUPPLEMENTAL INFORMATION

Supplemental Information includes Supplemental Experimental Procedures, sixteen movies, four figures, and one table and can be found with this article online at doi:10.1016/j.str.2010.04.008.

ACKNOWLEDGMENTS

W.A.H. and A.Y.H.Y. thank Usheer Kanjee and Taras Makhnevych for their help in some of the biochemical studies including the sedimentation velocity experiments. M.S.K. thanks Pragya Kapoor for performing crystallization trials. M.B. was a postdoctoral fellow of the Canadian Institutes of Health Research Training Program in Protein Folding: Principles and Diseases and also received a postdoctoral fellowship from the Sweden-America Foundation. This work was supported by grants from the Canadian Institutes of Health Research to W.A.H. (MOP-67210) and to H.S.C. (MOP-84281), and the Natural Sciences and Engineering Research Council of Canada to M.S.K. (327280-06). H.S.C. holds a Canada Research Chair.

Received: January 22, 2010
Revised: April 2, 2010
Accepted: April 16, 2010
Published: July 13, 2010

REFERENCES

Alliegro, M.C. (2000). Effects of dithiothreitol on protein activity unrelated to thiol-disulfide exchange: for consideration in the analysis of protein function with Cleland's reagent. Anal. Biochem. *282*, 102–106.

Atilgan, A.R., Durell, S.R., Jernigan, R.L., Demirel, M.C., Keskin, O., and Bahar, I. (2001). Anisotropy of fluctuation dynamics of proteins with an elastic network model. Biophys. J. *80*, 505–515.

Bahar, I., and Rader, A.J. (2005). Coarse-grained normal mode analysis in structural biology. Curr. Opin. Struct. Biol. *15*, 586–592.

Bahar, I., Atilgan, A.R., and Erman, B. (1997). Direct evaluation of thermal fluctuations in proteins using a single-parameter harmonic potential. Fold. Des. *2*, 173–181.

Bewley, M.C., Graziano, V., Griffin, K., and Flanagan, J.M. (2006). The asymmetry in the mature amino-terminus of ClpP facilitates a local symmetry match in ClpAP and ClpXP complexes. J. Struct. Biol. *153*, 113–128.

Bewley, M.C., Graziano, V., Griffin, K., and Flanagan, J.M. (2009). Turned on for degradation: ATPase-independent degradation by ClpP. J. Struct. Biol. *165*, 118–125.

Brooks, B.R., Janezic, D., and Karplus, M. (1995). Harmonic-analysis of large systems. 1. Methodology. J. Comput. Chem. *16*, 1522–1542.

Case, D.A. (1994). Normal mode analysis of protein dynamics. Curr. Opin. Struct. Biol. *4*, 285–290.

Choi, K.H., and Licht, S. (2005). Control of peptide product sizes by the energy-dependent protease ClpAP. Biochemistry *44*, 13921–13931.

CCP4 (Collaborative Computational Project, Number 4). (1994). The CCP4 suite: programs for protein crystallography. Acta Crystallogr. D Biol Crystallogr. *50*, 760–763.

Emsley, P., and Cowtan, K. (2004). Coot: model-building tools for molecular graphics. Acta Crystallogr. D Biol. Crystallogr. *60*, 2126–2132.

Gribun, A., Kimber, M.S., Ching, R., Sprangers, R., Fiebig, K.M., and Houry, W.A. (2005). The ClpP double ring tetradecameric protease exhibits plastic ring-ring interactions, and the N termini of its subunits form flexible loops that are essential for ClpXP and ClpAP complex formation. J. Biol. Chem. *280*, 16185–16196.

Hinsen, K. (1998). Analysis of domain motions by approximate normal mode calculations. Proteins *33*, 417–429.

Hinsen, K. (2008). Structural flexibility in proteins: impact of the crystal environment. Bioinformatics *24*, 521–528.

Ingvarsson, H., Mate, M.J., Hogbom, M., Portnoi, D., Benaroudj, N., Alzari, P.M., Ortiz-Lombardia, M., and Unge, T. (2007). Insights into the inter-ring plasticity of caseinolytic proteases from the X-ray structure of Mycobacterium tuberculosis ClpP1. Acta Crystallogr. D Biol. Crystallogr. *63*, 249–259.

Jennings, L.D., Bohon, J., Chance, M.R., and Licht, S. (2008a). The ClpP N-terminus coordinates substrate access with protease active site reactivity. Biochemistry *47*, 11031–11040.

Jennings, L.D., Lun, D.S., Medard, M., and Licht, S. (2008b). ClpP hydrolyzes a protein substrate processively in the absence of the ClpA ATPase: mechanistic studies of ATP-independent proteolysis. Biochemistry *47*, 11536–11546.

Joshi, S.A., Hersch, G.L., Baker, T.A., and Sauer, R.T. (2004). Communication between ClpX and ClpP during substrate processing and degradation. Nat. Struct. Mol. Biol. *11*, 404–411.

Kang, S.G., Maurizi, M.R., Thompson, M., Mueser, T., and Ahvazi, B. (2004). Crystallography and mutagenesis point to an essential role for the N-terminus of human mitochondrial ClpP. J. Struct. Biol. *148*, 338–352.

Kang, S.G., Dimitrova, M.N., Ortega, J., Ginsburg, A., and Maurizi, M.R. (2005). Human mitochondrial ClpP is a stable heptamer that assembles into a tetradecamer in the presence of ClpX. J. Biol. Chem. *280*, 35424–35432.

Keskin, O., Bahar, I., Flatow, D., Covell, D.G., and Jernigan, R.L. (2002). Molecular mechanisms of chaperonin GroEL-GroES function. Biochemistry *41*, 491–501.

Kim, D.Y., and Kim, K.K. (2008). The structural basis for the activation and peptide recognition of bacterial ClpP. J. Mol. Biol. *379*, 760–771.

Kim, M.K., Jernigan, R.L., and Chirikjian, G.S. (2002). Efficient generation of feasible pathways for protein conformational transitions. Biophys. J. *83*, 1620–1630.

Kundu, S., Melton, J.S., Sorensen, D.C., and Phillips, G.N., Jr. (2002). Dynamics of proteins in crystals: comparison of experiment with simple models. Biophys. J. *83*, 723–732.

Lawson, C. (1974). Solving Least Squares Problems (Englewood Cliffs, NJ: Prentice-Hall).

Licht, S., and Lee, I. (2008). Resolving individual steps in the operation of ATP-dependent proteolytic molecular machines: from conformational changes to substrate translocation and processivity. Biochemistry *47*, 3595–3605.

Lindahl, E., Azuara, C., Koehl, P., and Delarue, M. (2006). NOMAD-Ref: visualization, deformation and refinement of macromolecular structures based on all-atom normal mode analysis. Nucleic Acids Res. *34*, W52–W56. 10.1093/nar/gkl082.

Ma, J. (2005). Usefulness and limitations of normal mode analysis in modeling dynamics of biomolecular complexes. Structure *13*, 373–380.

Ma, J., Sigler, P.B., Xu, Z., and Karplus, M. (2000). A dynamic model for the allosteric mechanism of GroEL. J. Mol. Biol. *302*, 303–313.

Maglica, Z., Kolygo, K., and Weber-Ban, E. (2009). Optimal efficiency of ClpAP and ClpXP chaperone-proteases is achieved by architectural symmetry. Structure *17*, 508–516.

Marques, O., and Sanejouand, Y.H. (1995). Hinge-bending motion in citrate synthase arising from normal mode calculations. Proteins *23*, 557–560.

Martin, A., Baker, T.A., and Sauer, R.T. (2008). Diverse pore loops of the AAA+ ClpX machine mediate unassisted and adaptor-dependent recognition of ssrA-tagged substrates. Mol. Cell *29*, 441–450.

Maurizi, M.R., Clark, W.P., Katayama, Y., Rudikoff, S., Pumphrey, J., Bowers, B., and Gottesman, S. (1990a). Sequence and structure of Clp P, the proteolytic component of the ATP-dependent Clp protease of Escherichia coli. J. Biol. Chem. *265*, 12536–12545.

Maurizi, M.R., Clark, W.P., Kim, S.H., and Gottesman, S. (1990b). Clp P represents a unique family of serine proteases. J. Biol. Chem. *265*, 12546–12552.

Maurizi, M.R., Singh, S.K., Thompson, M.W., Kessel, M., and Ginsburg, A. (1998). Molecular properties of ClpAP protease of Escherichia coli: ATP-dependent association of ClpA and clpP. Biochemistry *37*, 7778–7786.

McRee, D.E. (1999). XtalView/Xfit—a versatile program for manipulating atomic coordinates and electron density. J. Struct. Biol. *125*, 156–165.

Minor, W., Cymborowski, M., Otwinowski, Z., and Chruszcz, M. (2006). HKL-3000: the integration of data reduction and structure solution—from diffraction images to an initial model in minutes. Acta Crystallogr. D Biol. Crystallogr. *62*, 859–866.

Miyashita, O., Onuchic, J.N., and Okamura, M.Y. (2003a). Continuum electrostatic model for the binding of cytochrome c2 to the photosynthetic reaction center from Rhodobacter sphaeroides. Biochemistry *42*, 11651–11660.

Miyashita, O., Onuchic, J.N., and Wolynes, P.G. (2003b). Nonlinear elasticity, proteinquakes, and the energy landscapes of functional transitions in proteins. Proc. Natl. Acad. Sci. USA *100*, 12570–12575.

Sprangers, R., Gribun, A., Hwang, P.M., Houry, W.A., and Kay, L.E. (2005). Quantitative NMR spectroscopy of supramolecular complexes: dynamic side pores in ClpP are important for product release. Proc. Natl. Acad. Sci. USA *102*, 16678–16683.

Szyk, A., and Maurizi, M.R. (2006). Crystal structure at 1.9A of E. coli ClpP with a peptide covalently bound at the active site. J. Struct. Biol. *156*, 165–174.

Thompson, M.W., and Maurizi, M.R. (1994). Activity and specificity of Escherichia coli ClpAP protease in cleaving model peptide substrates. J. Biol. Chem. *269*, 18201–18208.

Thompson, M.W., Singh, S.K., and Maurizi, M.R. (1994). Processive degradation of proteins by the ATP-dependent Clp protease from Escherichia coli. Requirement for the multiple array of active sites in ClpP but not ATP hydrolysis. J. Biol. Chem. *269*, 18209–18215.

Tirion, M.M. (1996). Large amplitude elastic motions in proteins from a single-parameter, atomic analysis. Phys. Rev. Lett. *77*, 1905–1908.

Vedadi, M., Lew, J., Artz, J., Amani, M., Zhao, Y., Dong, A., Wasney, G.A., Gao, M., Hills, T., Brokx, S., et al. (2007). Genome-scale protein expression and structural biology of Plasmodium falciparum and related Apicomplexan organisms. Mol. Biochem. Parasitol. *151*, 100–110.

Wang, J., Hartling, J.A., and Flanagan, J.M. (1997). The structure of ClpP at 2.3 A resolution suggests a model for ATP-dependent proteolysis. Cell *91*, 447–456.

Wojtyra, U.A., Thibault, G., Tuite, A., and Houry, W.A. (2003). The N-terminal zinc binding domain of ClpX is a dimerization domain that modulates the chaperone function. J. Biol. Chem. *278*, 48981–48990.

Yang, L., Song, G., Carriquiry, A., and Jernigan, R.L. (2008). Close correspondence between the motions from principal component analysis of multiple HIV-1 protease structures and elastic network modes. Structure *16*, 321–330.

Yu, A.Y., and Houry, W.A. (2007). ClpP: a distinctive family of cylindrical energy-dependent serine proteases. FEBS Lett. *581*, 3749–3757.

